Research Article

Limin Zhang, Liguang Zhu*, Caijun Zhang*, Pengcheng Xiao*, and Xingjuan Wang*

Influence of submerged entry nozzle on funnel mold surface velocity

https://doi.org/10.1515/htmp-2022-0247 received August 29, 2022; accepted October 05, 2022

Abstract: In this article, physical and numerical simulation of the flow field in flexible thin slab caster funnel mold at high casting speed is carried out with a five-hole submerged entry nozzle (FHSEN), and characteristics of the flow field on funnel mold liquid level under different casting speeds (4, 5, and 6 m·min⁻¹) and different submerged depths (130, 160, and 190 mm) are studied by comparing with the new submerged entry nozzle (NSEN) designed. Physical simulation is based on the funnel mold prototype. Numerical simulation is carried out based on FLUENT software, and industrial experiments of two kinds of submerged entry nozzle are also carried out. The results show that in the case of both physical and numerical simulation, the maximum surface velocity of the FHSEN funnel mold is 0.58 m·s⁻¹, and the funnel mold liquid level is prone to slag entrapment. The NSEN funnel mold' maximum surface velocity is 0.37 m·s⁻¹. Compared with the FHSEN, the NSEN funnel mold' maximum surface velocity decreases by 0.21 m·s⁻¹, and funnel mold surface velocity decreases significantly. Finally, the accuracy of simulation results is verified by industrial tests, and it is also show that NSEN can greatly reduce funnel mold surface velocity and probability of slag entrapment.

Keywords: funnel mold, submerged entry nozzle, surface velocity, simulation, industrial test

1 Introduction

The suitable shape of submerged entry nozzle (SEN) can better optimize the flow field and surface velocity of the funnel mold, which has a decisive influence on the quality of thin slab [1]. Since the high-efficiency continuous casting technology was put forward, casting speed is getting higher and higher, which also brings many production problems. For example, when the casting speed of flexible thin slab caster (FTSC) reaches 4 m·min⁻¹, the funnel mold liquid level fluctuation increases, which will cause a series of adverse effects, such as slag entrapment, resulting in the slab slag inclusion problem [2,3]. The uneven distribution of the liquid slag layer affects the lubricating effect of the slag and makes the slab prone to crack defects [4,5]. When the slag inclusion by the fluctuation of the liquid level is enriched at the solidified shell, it is easy to cause breakout and other production quality problems. All of these are related to the flow field distribution at the funnel mold liquid level, which is directly related to the shape of SEN [6,7]. However, the shape of SEN is limited by the size of funnel mold, and so when the SEN shape is flat and thin, it is more difficult to design the SEN for funnel mold. In the past, different shapes of the SEN were designed, typical shapes include "cownose," "dissipative," and "five-hole" [8]. The common design features of these SENs have the advantages of increasing the flow of molten steel, stabilizing the casting speed, and high service life [9]. However, the previous SENs are somewhat insufficient for the stability of the current high casting speed funnel mold flow field, their outlet area is

^{*} Corresponding author: Liguang Zhu, Hebei Provincial High-Quality Steel Continuous Casting Engineering Technology Research Center, Tangshan, Hebei 063000, China; School of Science and Engineering, Hebei University of Science and Technology, Shijiazhuang, Hebei 050018, China, e-mail: zhuliguang@ncst.edu.cn

^{*} Corresponding author: Caijun Zhang, Hebei Provincial High-Quality Steel Continuous Casting Engineering Technology Research Center, Tangshan, Hebei 063000, China; College of Metallurgy and Energy, North China University of Science and Technology, Tangshan, Hebei 063009, China, e-mail: zhangcaijun@126.com

^{*} Corresponding author: Pengcheng Xiao, Hebei Provincial High-Quality Steel Continuous Casting Engineering Technology Research Center, Tangshan, Hebei 063000, China; College of Metallurgy and Energy, North China University of Science and Technology, Tangshan, Hebei 063009, China, e-mail: 376975266@qq.com

^{*} Corresponding author: Xingjuan Wang, Hebei Provincial High-Quality Steel Continuous Casting Engineering Technology Research Center, Tangshan, Hebei 063000, China; College of Metallurgy and Energy, North China University of Science and Technology, Tangshan, Hebei 063009, China, e-mail: wxingjuan@ncst.edu.cn Limin Zhang: Hebei Provincial High-Quality Steel Continuous Casting Engineering Technology Research Center, Tangshan, Hebei 063000, China; College of Metallurgy and Energy, North China University of Science and Technology, Tangshan, Hebei 063009, China

small, and the outlet angle and molten steel flow velocity are large, which leads to the upward movement of the swirl zone and the increase of the surface velocity, which easily leads to slag entrapment. Therefore, this article designs a new submerged entry nozzle (NSEN), whose design idea is to increase the outlet area and reduce the outlet angle. This design has the following advantages: large amount of molten steel passing through the outlet, low flow velocity of molten steel at the outlet, and reduced kinetic energy of collision between molten steel at the outlet and narrow face of funnel mold. Finally, the surface velocity of the upper reflux at the liquid level is reduced, and the purpose of controlling the shear slag entrapment at the liquid level is achieved.

To study the application effect of the NSEN, based on the FTSC funnel mold, this article focuses on the use of FLUENT software to numerical simulation of the funnel mold flow field of the five-hole submerged entry nozzle (FHSEN) and NSEN, respectively, and make a comparison. The specific scheme is to study and compare the characteristics of funnel mold liquid level flow field under the conditions of constant submerged depth of 130 mm; casting speeds of 4, 5, and 6 m·min⁻¹; constant casting speed of 6 m·min⁻¹; and submerged depths of 130, 160, and 190 mm. Finally, the simulation results are compared with industrial tests. The results show that compared with the FHSEN, the NSEN has the characteristics of stable liquid level, low surface velocity, and not easy to slag entrapment.

2 Experimental and simulation

2.1 Funnel mold and submerged entry nozzle model description

The model in this study uses FTSC funnel mold, and its size is 1,520 mm \times 73 mm \times 1,200 mm (width \times thickness \times height). The middle part is funnel shaped, the width of the funnel area is 800 mm, the height is 900 mm, and the lower part is a rectangular area of 300 mm. The funnel mold has the characteristics of "narrow at both ends and wide in the middle." See Figure 1.

The SEN used in the model is FHSEN and NSEN. The main characteristics of the FHSEN are that the upper part is cylindrical, and the transition from the lower end of the cylinder to the lower end of the SEN is in a flat fan shape, the outlet at both sides of the FHSEN is 45°, and there is a

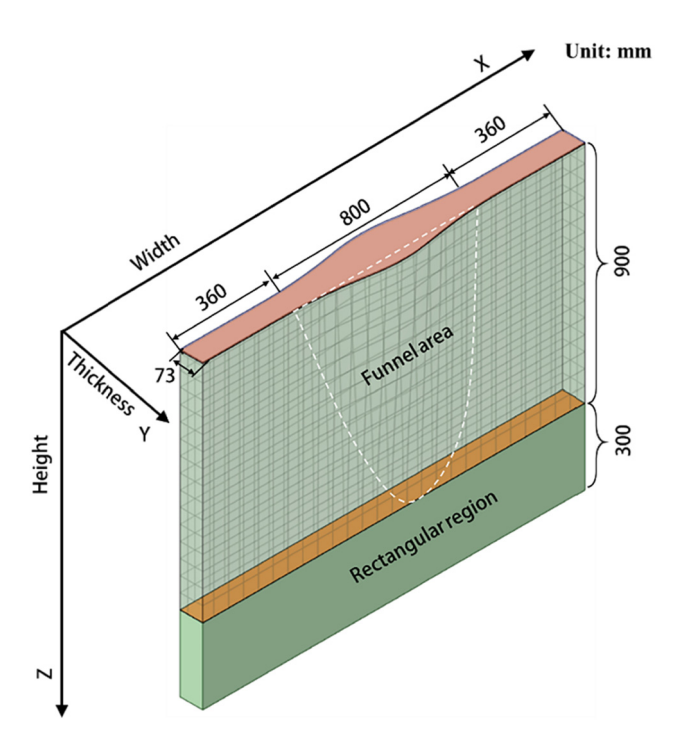


Figure 1: Funnel mold model.

notch dam in the middle and a 33 mm dam between the outlet at both ends and the vertical 18 mm rectangular outlet in the middle, as shown in Figure 2(a). The main difference between the NSEN and FHSEN is that the lower end of the SEN is a through vertical downward outlet, and the outlet area at both sides is large, while the outlet area at the middle connecting part is small. The fluid domain of the NSEN is shown in Figure 2(b).

2.2 Physics simulation

The physical flow field verification of the FHSEN and NSEN is consistent in principle. To save time and cost of making experiment equipment, the FHSEN is selected as the representative of the physical experiment to verify the accuracy of the numerical simulation results, and the NSEN is directly analyzed by numerical simulation.

The experiment adopts a 1:1 full-scale water physical model. The flow of molten steel in the funnel mold is mainly affected by viscous force, gravity, and inertial force [10,11]. Therefore, we can only consider the Equality of Froude numbers, and so equation (1) is derived.

$$\frac{u_{\rm p}^2}{gl_{\rm n}} = \frac{u_{\rm m}^2}{gl_{\rm m}},\tag{1}$$

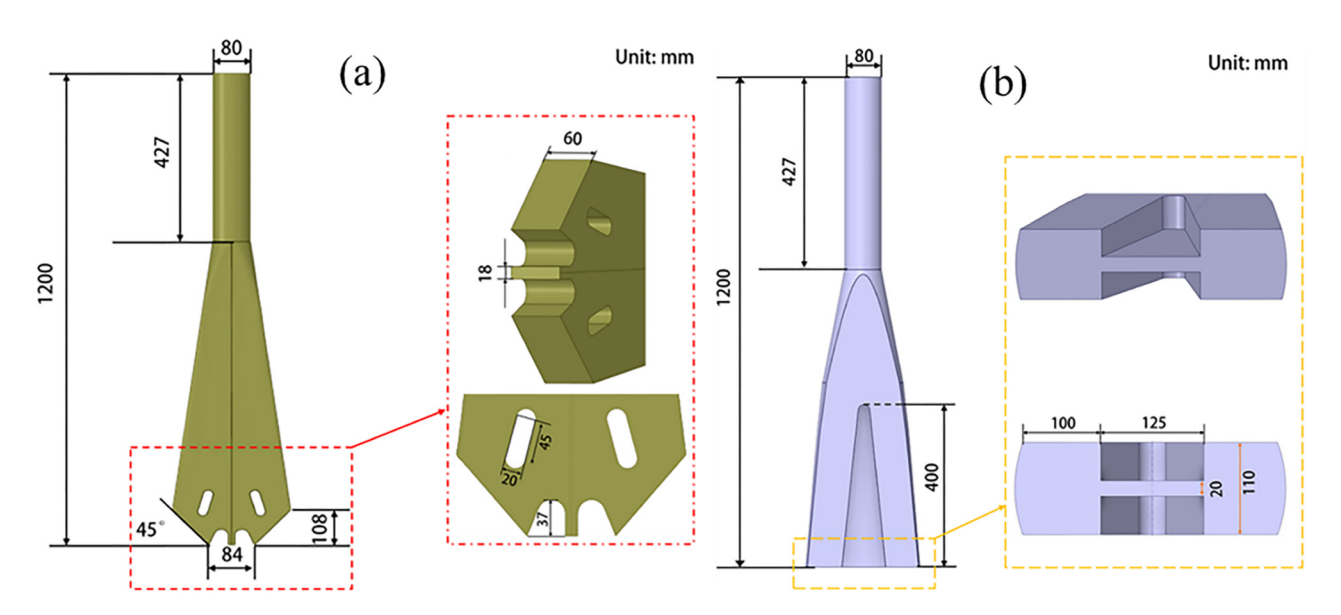


Figure 2: SEN shape: (a) FHSEN and (b) NSEN.

where u_p is the molten steel flow velocity, $m \cdot s^{-1}$; u_m is the velocity of water, $m \cdot s^{-1}$; g is the acceleration of gravity, $m \cdot s^{-1}$; l_p is the length of the actual funnel mold, m; and l_m is the length of model funnel mold, m.

A 1:1 water physical model made of plexiglass material was prepared in the experiment, and the water flow was controlled by a nozzle valve with closed-loop stability control, as shown in Figure 3(a) and (b). In addition, the ultrasonic flowmeter and the water pump control system are used to control the casting speed. LGY-II propeller speedometer is used to measure surface velocity because it is a portable ultra-small speedometer using advanced electronic technology, sensing technology, and computer software and hardware technology, see Figure 3(c). China's national invention patent has been obtained and is widely used by China Water Resources Bureau. The measurement method is as follows: under the condition that the experimental state is stable, the propeller can be placed at the position completely covered by the liquid level, and then the measurement will start, the LGY-II propeller speedometer will automatically continuously measure for three times, and then the average value of the surface velocity is displayed on the screen. The seven measuring points are shown in Figure 3(d). The whole data acquisition process is automatically acquired by computer and processed by professional software.

The water physical model experiment was carried out for the FHSEN under two different process conditions. The two process conditions are as follows:

(1) Keep the submerged depth of the FHSEN constant at 130 mm, and study the influence of different casting

- speeds (4, 5, and 6 m·min⁻¹) on the liquid level flow field of the funnel mold.
- (2) Keep the casting speed constant at 6 m·min⁻¹, and study the influence of different submerged depths (130, 160, and 190 mm) on the liquid level flow field of the funnel mold.

In addition, to check the influence of the surface velocity on slag entrapment, on the basis of the aforementioned experimental scheme, the oil—water two-phase experiment was carried out with the vacuum pump oil prepared according to the principle of kinematic viscosity similarity to replace the slag, and the vacuum pump oil thickness is 10 mm.

2.3 Numerical simulation

In this article, the flow field of the funnel mold is numerically simulated by FLUENT software. Due to the complex flow behavior of molten steel in the funnel mold, to establish a suitable mathematical model, the following assumptions are made [12,13]: (1) The molten steel flow in the funnel mold is viscous and incompressible. (2) The density difference after solidification of the slab is ignored, and the molten steel in the funnel mold is treated as a homogeneous medium. (3) The influence of factors such as funnel mold vibration on the flow field is not considered. (4) The funnel mold wall is defined as a nonslip boundary. (5) The influence of the solidified shell on the funnel mold is ignored.

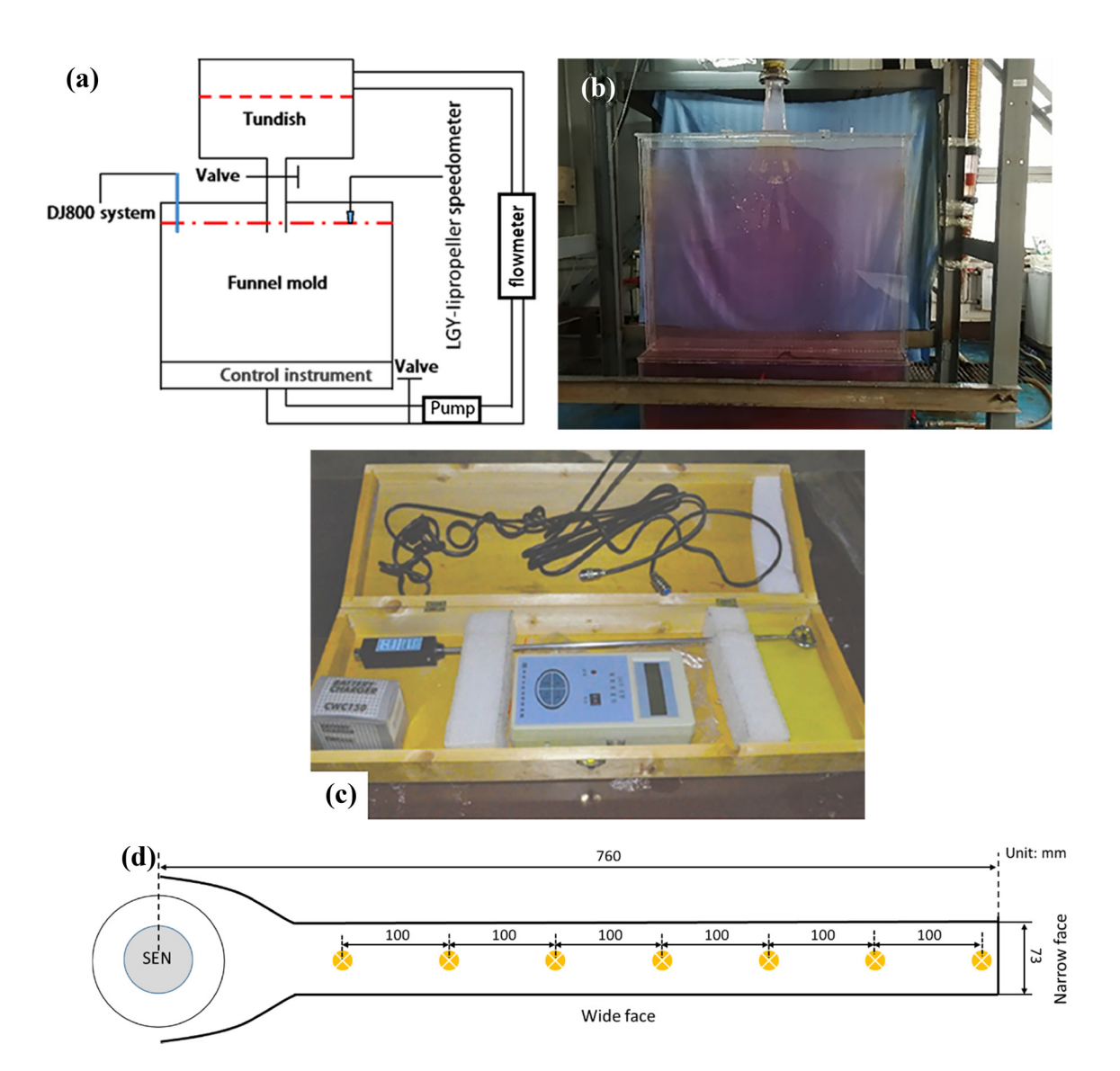


Figure 3: Physical experiment: (a) schematic diagram of physical experiment, (b) physical experimental model, (c) LGY-II propeller speedometer, and (d) measuring position.

2.3.1 Control equation

Molten steel in funnel mold is a three-dimensional incompressible fluid, and its flow control equations include continuity equation, momentum equation, and turbulence model equation. The turbulence model used in this article is the standard $k-\varepsilon$ equation, and the specific equations (equations (2)–(7)) [14,15] are presented as follows:

Continuity equation:

$$\frac{\partial \rho u_i}{\partial x_i} = 0.$$
(2)

N-S equation:

$$\frac{\partial(\rho u_{i}u_{j})}{\partial x_{j}} + \frac{\partial(\rho u_{i})}{\partial t} = -\frac{\partial P}{\partial x_{i}} + \frac{\partial}{\partial x_{j}} \left[\mu_{\text{eff}} \left[\frac{\partial \mu_{i}}{\partial x_{j}} + \frac{\partial \mu_{j}}{\partial x_{i}} \right] \right] + \rho g_{i} + F_{i},$$
(3)

where

$$\mu_{eff} = \mu_l + \mu_t = \mu_l + \rho C_{\mu} k^2 / \varepsilon. \tag{4}$$

where μ_t is determined by the two-equation turbulence model proposed by Launder and Spalding. When the $k-\varepsilon$ model is used:

$$\mu_t = \rho C_\mu k^2 / \varepsilon. \tag{5}$$

Turbulent kinetic energy equation:

$$\rho u_j \frac{\partial k}{\partial x_j} = \frac{\partial}{\partial x_j} \left[\left(u_l + \frac{u_t}{\sigma_k} \right) \frac{\partial k}{\partial x_j} \right] + \mu_t \frac{\partial u_j}{\partial x_j} \left[\frac{\partial u_i}{\partial x_j} + \frac{\partial u_j}{\partial x_i} \right]$$

$$- \rho \varepsilon.$$
(6)

Dissipation rate of turbulent kinetic energy:

$$\rho u_k \frac{\partial \varepsilon}{\partial x_k} = \frac{\partial}{\partial x_k} \left[\left(u_l + \frac{u_t}{\sigma_{\varepsilon}} \right) \frac{\partial \varepsilon}{\partial x_k} \right] + \frac{C_1 \varepsilon}{k} \mu_t \frac{\partial u_j}{\partial x_j} \left[\frac{\partial u_i}{\partial x_j} + \frac{\partial u_j}{\partial x_i} \right] - \frac{C_2 \rho \varepsilon^2}{k},$$
(7)

where u_i and u_i are the time-averaged velocity of the turbulent flow, m·s⁻¹; x_i and x_i are the coordinate variables; ρ is the molten steel density, kg·m⁻³; P is the pressure acting on the fluid micro-element, Pa; $\mu_{\rm eff}$ is the effective viscosity coefficient, Pa·s; u_1 and u_t are the viscosity coefficients of laminar flow and turbulent flow, respectively; g_i is the acceleration due to gravity in the idirection; and F_i is the source term.

In the numerical simulation, the coefficients of the aforementioned formulas are the values recommended by Launder [16]: C_1 = 1.44, C_2 = 1.92, C_{μ} = 0.09, σ_k = 1.0, and σ_{ε} = 1.3.

2.3.2 Multiphase model

In the simulation of the funnel mold steel/slag interface, the volume of fluid (VOF) method was used to track the steel/slag interface, define the fluid volume fraction in the space grid of the moving interface, construct the development equation of the fluid volume fraction, track the changes of the interface, determine the position and shape of the steel/slag interface, and thus construct the steel/slag interface.

The VOF model was employed to solve the multiphase system steel-slag. This scheme performs the calculation of the interface between the phases (p and q) present at each cell, based on their fraction as follows [17]:

$$\rho_{\text{mix}} = \alpha_p \rho_p + (1 - \alpha_q) \rho_p, \tag{8}$$

$$\mu_{\text{mix}} = \alpha_p \mu_p + (1 - \alpha_q) \mu_p, \tag{9}$$

where ρ_{mix} is the mixed phase density, kg·m⁻³; μ_{mix} is the mixed phase viscosity, Pa s; α_p , α_q are the volume fraction of the $p_{\rm th}$ and $q_{\rm th}$ phases, respectively, %; and μ_p is the viscosity fraction of the $p_{\rm th}$ phase, %.

A unique continuity equation for the transient system is derived depending on the number of phases; therefore, equation (10) is divided by the amount of phase q in the cell. The mass exchange between phases can be modeled by introducing an additional source term (S_{α_a}) [18].

$$\frac{\partial}{\partial t}(\alpha_q \rho_q) + \nabla \cdot (\alpha_q \rho_q \overrightarrow{v}) = S_{\alpha_q} + \sum_{p=1}^n (\dot{m}_{pq} - \dot{m}_{qp}), \quad (10)$$

where ρ_q and ρ_q are the density fraction of the $q_{\rm th}$ and $p_{\rm th}$ phases, respectively, kg·m⁻³; and \dot{m}_{pq} , \dot{m}_{qp} are the mass exchange between p and q phases, respectively, kg/s.

The VOF model solves a single set of momentum transfer equations when two or more phases coexist in the cell.

$$\frac{\partial}{\partial t} (\rho_{\text{mix}} \overrightarrow{v}) + \nabla \cdot (\rho_{\text{mix}} \overrightarrow{v} \overrightarrow{v})$$

$$= -\nabla p + \nabla [\mu_{\text{miv}} (\nabla \overrightarrow{v} + \nabla \overrightarrow{u})] - S_{S} + S_{\sigma}, \tag{11}$$

where S_s and S_{σ} are the exchange rate of the stress tensor.

The tracking of the interface is accomplished by an implicit method, which solves the face fluxes (\dot{m}) in each grid cell through equation (12):

$$\frac{\alpha_q^{n+1}\rho_q^{n+1} - \alpha_q^n \rho_q^n}{\partial t} V + \sum_f (\rho_q^{n+1} U_f^{n+1} \alpha_{qf}^{n+1})
= \left[S_{\alpha q} + \sum_{p=1}^n (\dot{m}_{pq} - \dot{m}_{qp}) \right] V.$$
(12)

2.3.3 Domain and mesh

To reduce the calculation time, according to the symmetry of the flow in the funnel mold, the calculation area is taken as 1/4 of the funnel mold flow area for simulation calculation. To avoid the influence of reflux on the calculation accuracy, the length of the calculating funnel mold domain was determined to be 2,200 mm by trial calculation. The MESH module of Ansys software is used to divide the model, tetrahedral unstructured cells and hexahedral cells were used, and the funnel mold liquid level domain was encrypted. The mesh-independent verification of the calculation results was carried out and the cells of the FHSEN funnel mold model and the NSEN funnel mold model were determined to be about 1.1million and 0.98 million, respectively. See Figure 4.

2.3.4 Boundary conditions

Turbulence intensity *I* [19]:

$$I = 0.16 \text{Re}^{-\frac{1}{8}} = 0.16 \left(\frac{\nu_{\text{inlet}} D_{\text{H}}}{V} \right)^{1/8}$$
 (13)

Determination of turbulent kinetic energy *K* and turbulent kinetic energy dissipation rate ε [20]:

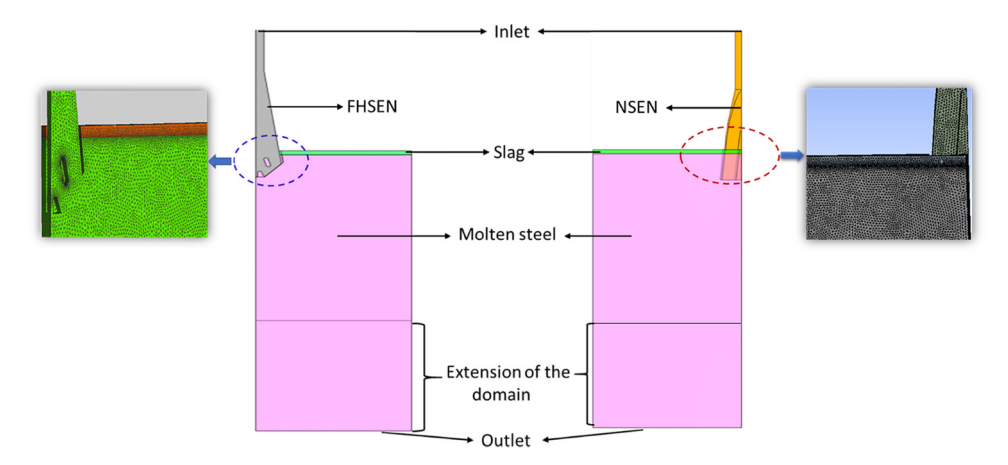


Figure 4: Funnel mold models and local cells.

$$K = \frac{3}{2}(\nu_{\text{inlet}}I)^2,\tag{14}$$

$$\varepsilon = c_{\mu}^{3/4} \frac{k^{3/2}}{I}.\tag{15}$$

The Re is the Reynolds number, the hydraulic diameter of $D_{\rm H}$ is 80 mm, and V is the kinematic viscosity of molten steel.

According to the casting speed (4, 5, and 6 m·min⁻¹), the inlet velocity of the funnel mold SEN can be determined. ε and K can be calculated by equations (14) and (15), respectively. In the VOF model, the thickness of the slag layer above the molten steel level of the funnel mold is set as 30 mm, and the rest is molten steel. A pressure outlet condition was chosen on the domain bottom at the funnel mold outlet as 0 Pascal gauge pressure. The non-slip boundary condition is used for the wall surface, and the standard wall function method is used for the near-wall area.

2.3.5 Computing approach

The control equations were discretized and solved by the computational segregated-iterative method in ANSYS FLUENT with a second-order upwind scheme. In the VOF model, the nonlinear control equations were linearized using the implicit approach. The body weighted scheme was used for pressure interpolation; this scheme computes the cell-face pressure by assuming that the normal gradient of the difference between pressure and body forces is constant. The algorithm used for pressure–velocity coupling is known as SIMPLEC. The transient calculation is also carried out, and convergence criterion was obtained when the residuals of the output variables reached values equal or smaller than 0.0001. The transient, two-phase

model was started at time $= 0 \, s$ and run for $100 \, s$. The flow was allowed to develop for 15 s, and then a further time of data was used for compiling time-averages.

2.3.6 Simulation scheme

The established mathematical simulation objects are the three-dimensional thin slab funnel mold combined with the FHSEN and NSEN, respectively. The simulation scheme is designed as follows:

- (1) The submerged depth is constant at 130 mm, and the casting speed is selected as 4, 5, and 6 m⋅min⁻¹, respectively.
- (2) The casting speed is constant at 6 m·min⁻¹, and the submerged depth is 130, 160, and 190 mm.

Parameters used in physical and numerical simulations are presented in Table 1.

3 Results and discussion

3.1 Physical and numerical simulation of FHSEN

3.1.1 Influence of casting speed on the funnel mold surface velocity

When FHSEN submerged depth is constant at 130 mm, physical simulation and numerical simulation of the funnel mold surface velocity under the conditions of 4, 5, and 6 m·min⁻¹ are carried out. Figure 5 shows that the

Table 1: Parameters used in physical and numerical simulations

Item	Value
Funnel mold size diameter (mm)	1,520 × 73 × 2,200
Five-hole nozzle inlet diameter (mm)	80
NSEN inlet (mm)	80
Submerged depth (mm)	130/160/190
Casting speed (m·min ⁻¹)	4/5/6
Molten steel density (kg⋅m ⁻³)	7,020
Molten steel viscosity (Pa·s)	0.0064
Slag/molten steel surface tension $(N \cdot m^{-1})$	1.3
Liquid slag density (kg⋅m ⁻³)	2,700
Liquid slag viscosity (Pa·s)	0.18
Water density (kg⋅m ⁻³)	1,000
Water viscosity (Pa⋅s ⁻¹)	0.001
Vacuum pump oil density (kg·m ⁻³)	866.8
Vacuum pump oil viscosity (Pa·s)	0.101
Vacuum pump oil thickness (mm)	10

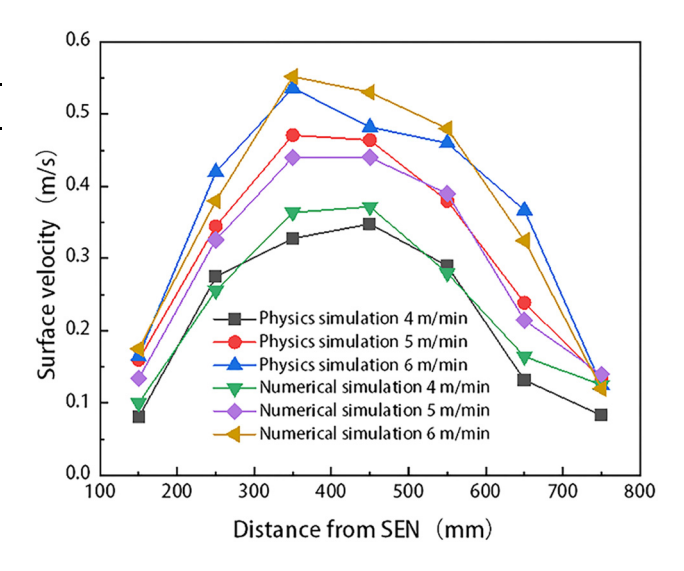


Figure 5: Influence of casting speed on funnel mold surface velocity.

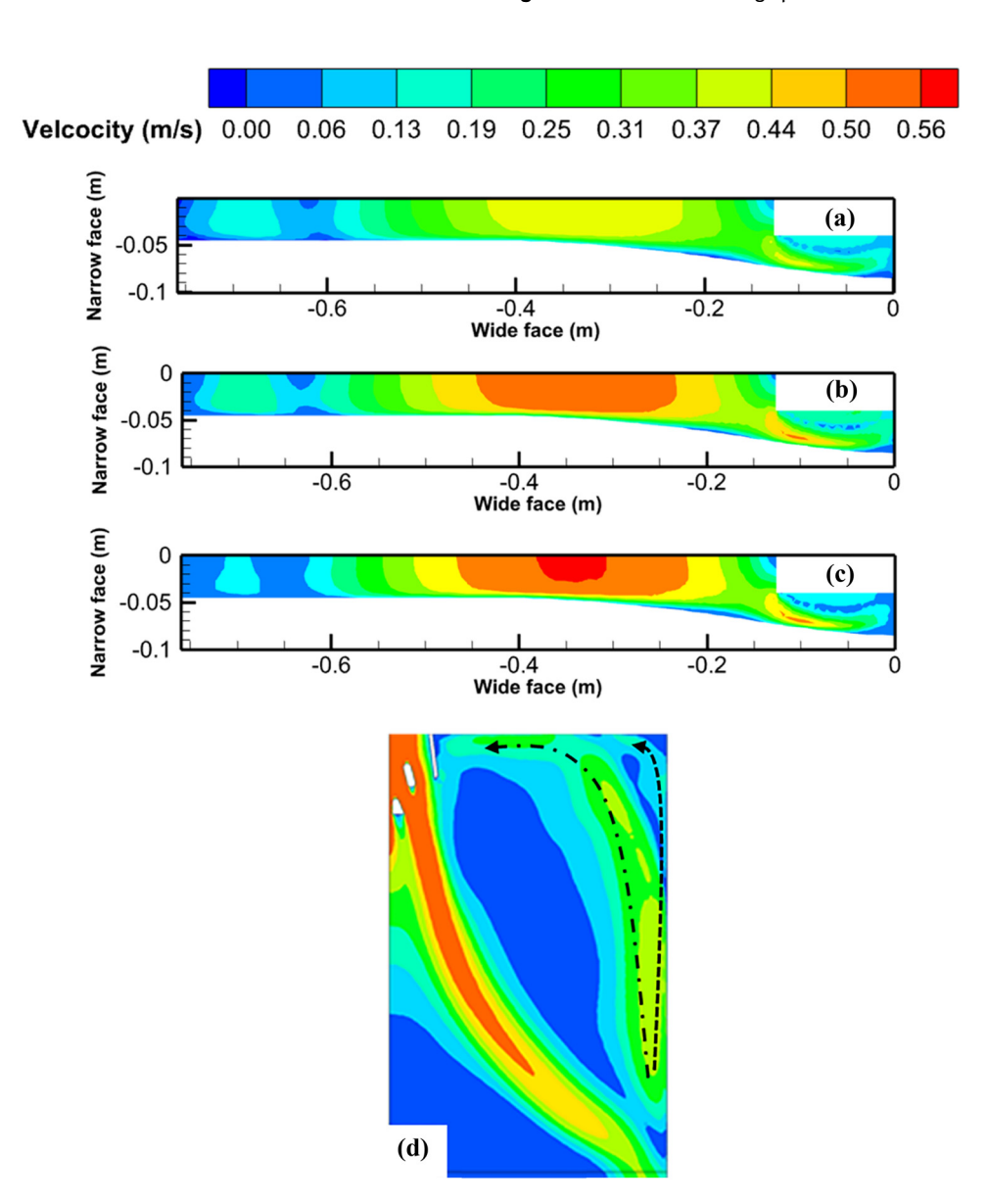


Figure 6: Surface velocity distribution of funnel mold at different casting speed and image of fluid flow in the funnel mold: (a) 4 m·min⁻¹, (b) 5 m·min⁻¹, (c) 6 m·min⁻¹, and (d) image of different paths flowing upward.

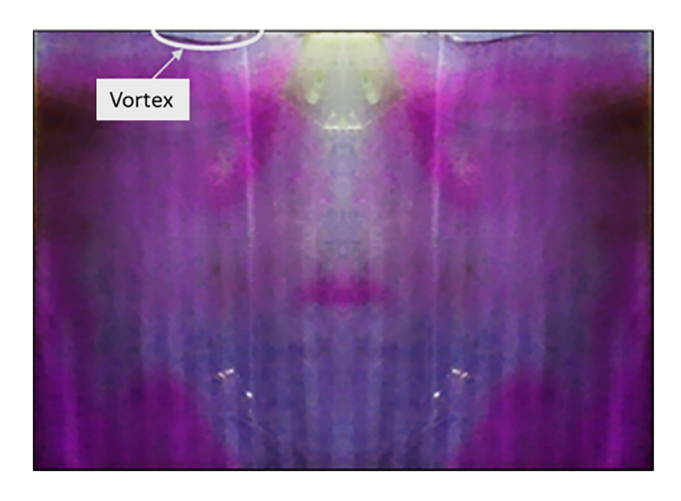


Figure 7: Typical liquid level fluctuation.

surface velocity of each measuring point in the funnel mold increases with the increase of the casting speed, whether in physical simulation or numerical simulation. At the centerline of the funnel mold wide face, along the FHSEN to the funnel mold narrow face, the surface velocity increases first and then decreases. At about 350 mm away from the FHSEN, the maximum surface velocity is obtained at all casting speeds, and its maximum value fluctuates between 0.35 and 0.56 m·s $^{-1}$. The reason is that

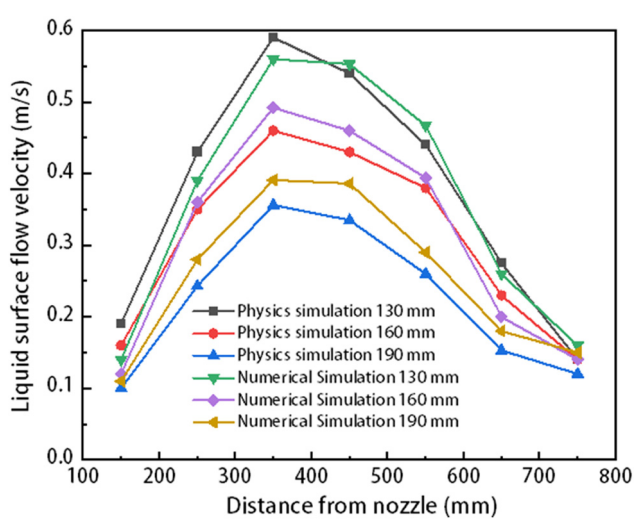


Figure 8: Influence of different submerged depths on surface velocity.

when the casting speed increases, the amount of molten steel flowing from the FHSEN outlet increases per unit time, the kinetic energy of the stream increases, the kinetic energy of the upward flow formed after colliding with the narrow face also increases, the average liquid level turbulent kinetic energy also increases, the liquid level is active, the velocity of the final upflow when it

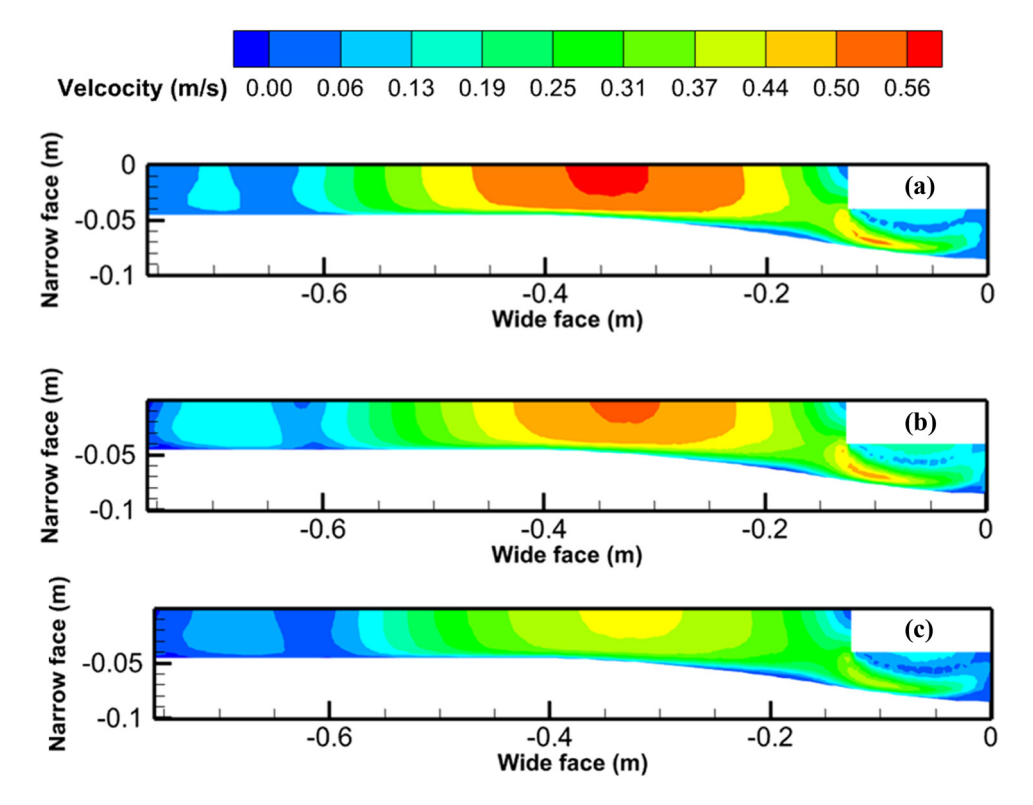


Figure 9: Surface velocity of different submerged depths at 6 m·min⁻¹ casting speed: (a) 130 mm, (b) 160 mm, and (c) 190 mm.



Figure 10: Funnel mold liquid level slag entrapment diagram: (a) physical simulation and (b) numerical simulation (30 s).

reaches the liquid level of the funnel mold increases, and the probability of slag entrapment also increases. In addition, when the casting speed is 4, 5, and $6\,\mathrm{m\cdot min^{-1}}$, the curve trend of physical simulation value and numerical simulation value is basically consistent, which is in good agreement.

When the casting speed is 4–6 m·min⁻¹, the maximum range of surface velocity is 0.38–0.56 m·s⁻¹, as shown in Figure 6, and when the minimum casting speed is 4 m·min⁻¹, the liquid level near the SEN fluctuates greatly, and slag entrapment is easy to occur at this position, as shown in Figure 7.

Figure 6 shows one thing in common that there are two obvious areas of high speed on the liquid level, one is the region with the highest surface velocity near SEN, and the other is the region with relatively low surface velocity near the narrow surface of funnel mold. The reason is that after the molten steel from SEN impinging on the narrow face of the funnel mold, the increasing flow is mainly divided into two parts, one part flows upward along the narrow face of the funnel mold, and finally, it flows out on the liquid level close to the narrow face of the funnel mold. Another large part of the diverter flows upward at a large angle to the narrow face of the funnel mold and finally exits at the liquid level near the SEN. A typical flow path image is shown in Figure 6(d).

Therefore, when the SEN submerged depth is constant at 130 mm and the casting speed is 4-6 m·min⁻¹, there will be obvious vortex phenomenon on the funnel mold liquid level at the funnel mold liquid level near the SEN and narrow face, which is also shown in Figure 7. The higher the horizontal surface velocity of the funnel mold liquid level, the more active the steel/slag interface, which is beneficial to slag melting. However, if the horizontal surface velocity of the funnel mold is too high, the liquid level will be unstable, and it is easy to cause slag entrapment. Therefore, adopting a larger submerged depth or reducing the casting speed is beneficial to reduce the surface velocity and reduce the probability of slag entrapment. However, if the submerged depth is too deep, a series of adverse effects will be produced, such as being unfavorable for the floating of inclusions and the liquid core being too long [21].

3.1.2 Influence of FHSEN submerged depths on funnel mold surface velocity

At a constant casting speed of 6 m·min⁻¹, when the FHSEN submerged depth is 130, 160, and 190 mm, respectively. The physical simulation value of the funnel mold surface velocity is in good agreement with the numerical simulation value, see Figure 8. At the same time, the surface velocity of each measuring point at the same position in the funnel mold decreases with the increase in the submerged depth, whether it is physical simulation or numerical simulation. Because when the FHSEN submerged depth increases, the distance from the upflow formed by the funnel mold narrow face to the liquid level increases, the kinetic energy loss of the upwelling flow increases as it moves to the liquid level, and the speed of the upward flow formed when it reaches the liquid level becomes smaller. The shallower the submerged depth of the FHSEN, the closer the upper swirl zone is to the funnel mold liquid level, and the stronger the upper backflow impinges on the liquid level. At the same submerged depth, the surface velocity increases first and then decreases with the increase in the distance from the FHSEN. Both physical simulation results and numerical simulation results show that the

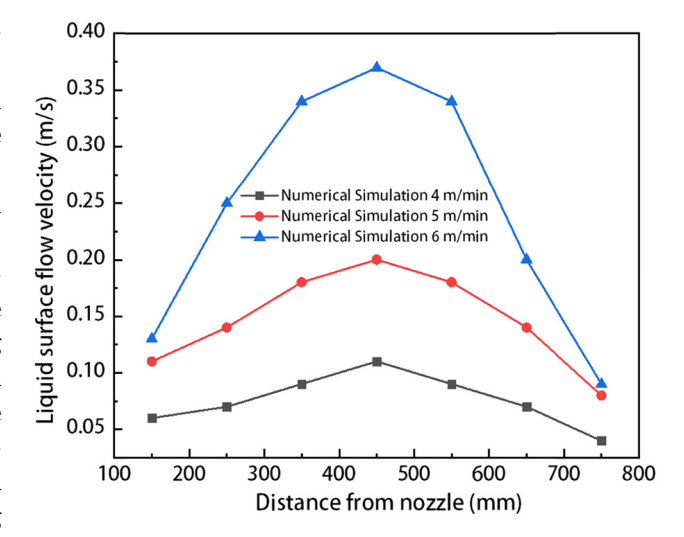


Figure 11: Influence of the casting speed on funnel mold surface velocity.

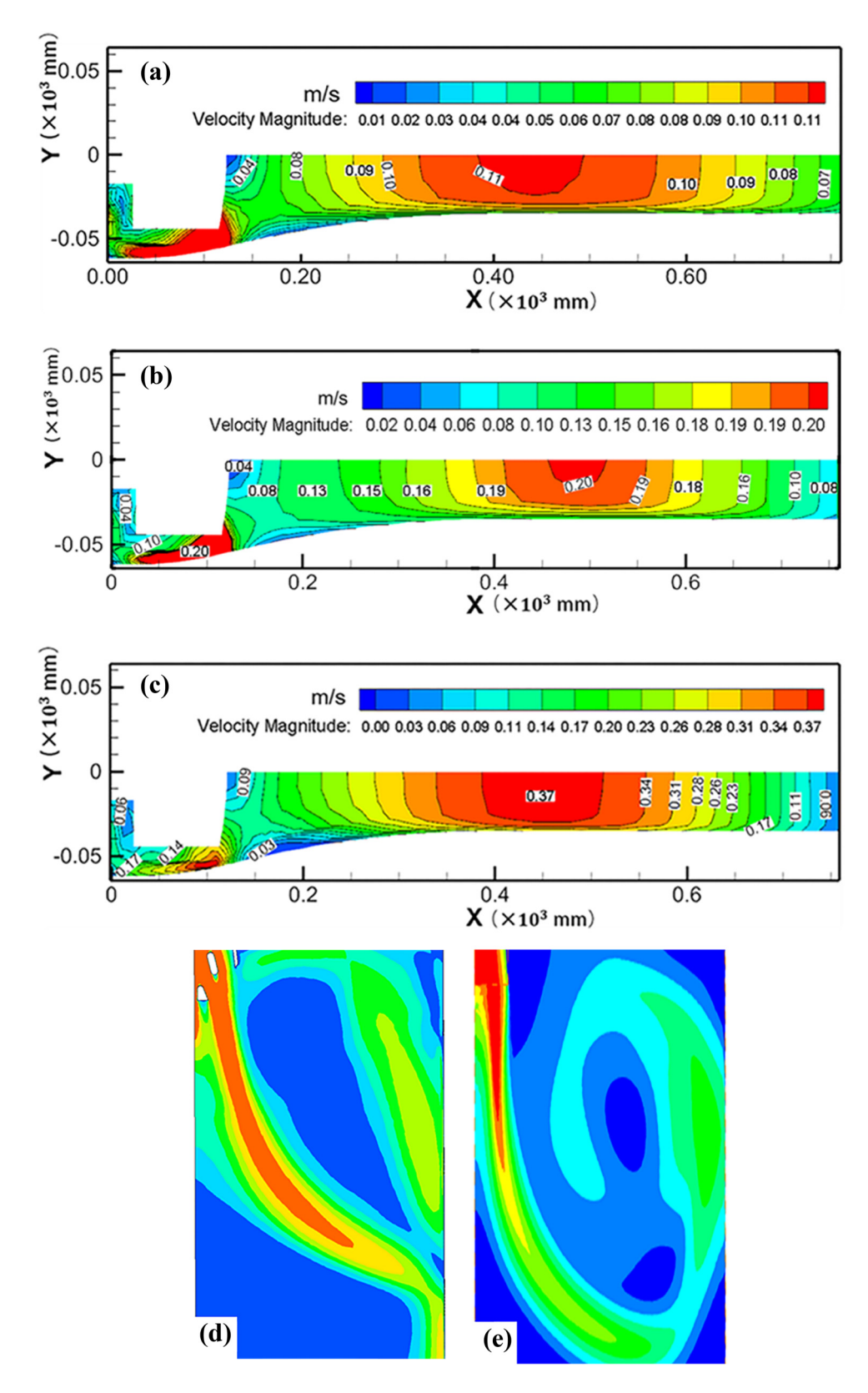


Figure 12: Surface velocity distribution of funnel mold at different casting speeds and cloud image of fluid flow in the funnel mold: (a) 4 m·min⁻¹, (b) 5 m·min⁻¹, (c) 6 m·min⁻¹, (d) FHSEN, and (e) NSEN.

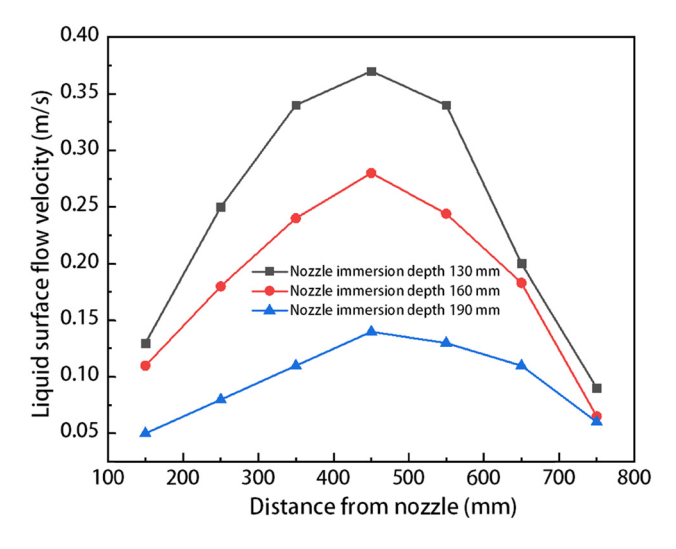


Figure 13: Influence of different submerged depths on surface velocity.

surface velocity reaches its maximum value when it is about 350 mm away from the FHSEN. Figure 9 shows in detail the surface velocity at different submerged depths at a constant casting speed of 6 m·min⁻¹. Figure 9 shows that with the increase in the depth of the SEN, the drop of the funnel mold surface velocity decreases. When the depth of the SEN increases from 130 to 190 mm, the maximum flow surface velocity of the funnel mold decreases from 0.58 to 0.34 m·s⁻¹. The numerical simulation results show that the maximum surface velocity decreases from 0.56 to 0.39 m·s⁻¹. Figure 8 shows that at the meniscus surface of the narrow face of the funnel mold, the gap between the surface velocity and the adjacent measuring points decreases because the flow stocks rising along the narrow face of the funnel mold flow out of the liquid level here, leading to the increase in the flow rate here.

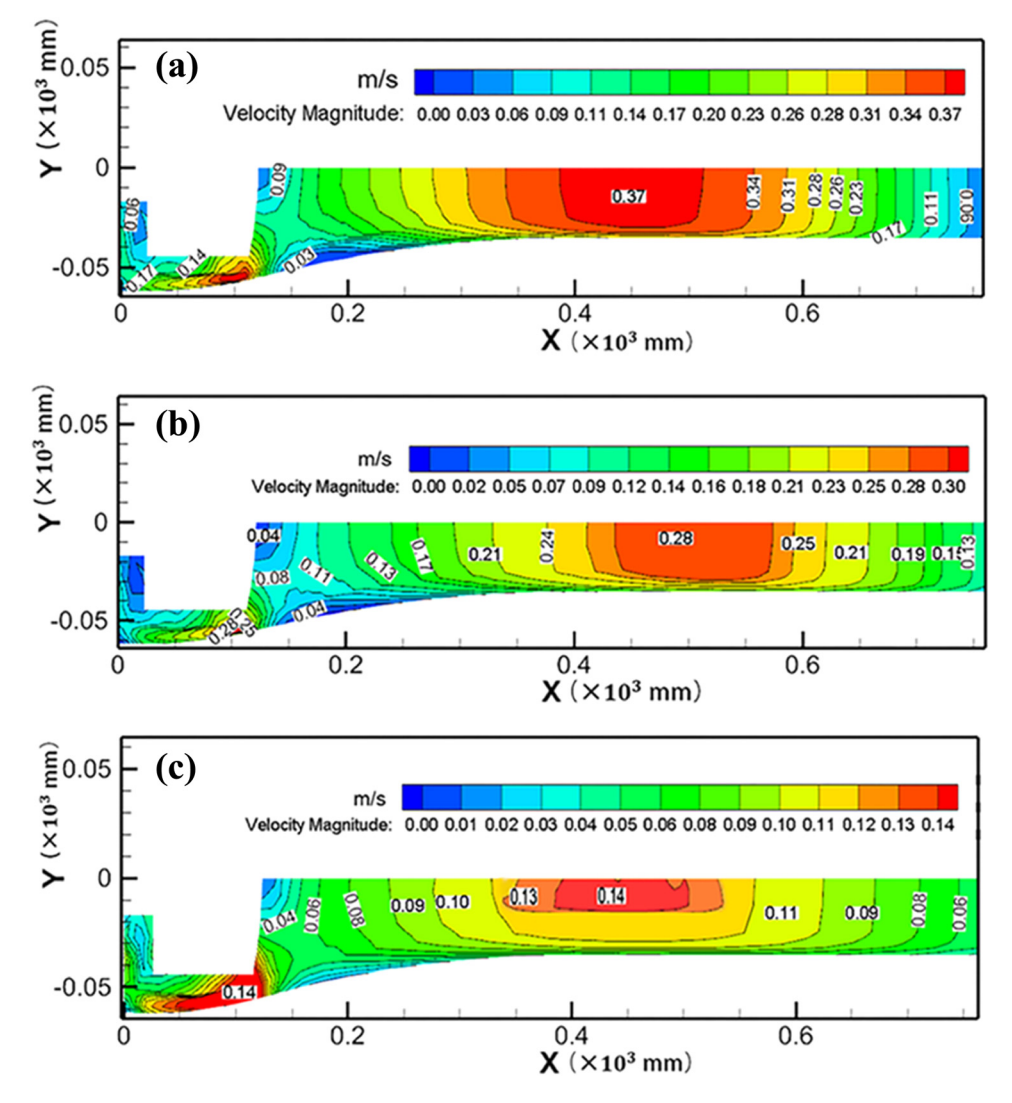


Figure 14: Surface velocity of different submerged depths at 6 m·min⁻¹ casting speed: (a) 130 mm, (b) 160 mm, and (c) 190 mm.

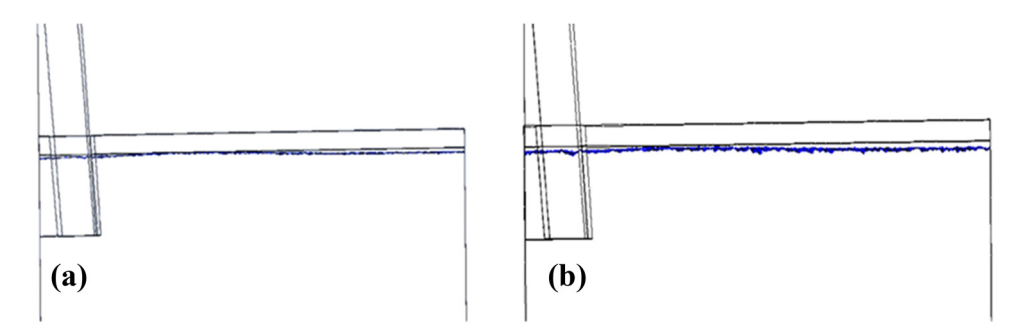


Figure 15: Funnel mold liquid level slag entrapment diagram: (a) 30 s and (b) 60 s.



Figure 16: NSEN for experiment.

It can be seen that the physical simulation results are in good agreement with the numerical simulation results. The higher the casting speed, the deeper the submerged depth should be, which is beneficial to reduce the probability of liquid level fluctuation.

When the FHSEN submerged depth is 190 mm, under the casting speed of 4 m·min⁻¹, in the oil and water physical simulation, Figure 10(a) shows that the direction of the surface velocity vector points from the funnel mold narrow face to the FHSEN, and the oil on the liquid level close to the narrow side follows the flow of molten steel and is pushed to the center between the FHSEN and the narrow face. Since the liquid level velocity is within the maximum range, the oil is sheared into the water, and the phenomenon of slag entrapment occurs. The VOF simulation results also show that when the volume fraction of slag is 0.05%, the phenomenon of slag entrapment occurs on the liquid level, see Figure 10(b).

Through the physical simulation and numerical simulation results of the FHSEN, it can be seen that when the FHSEN is used, the maximum submerged depth is 190 mm and the minimum casting speed is 4 m·min⁻¹. The liquid

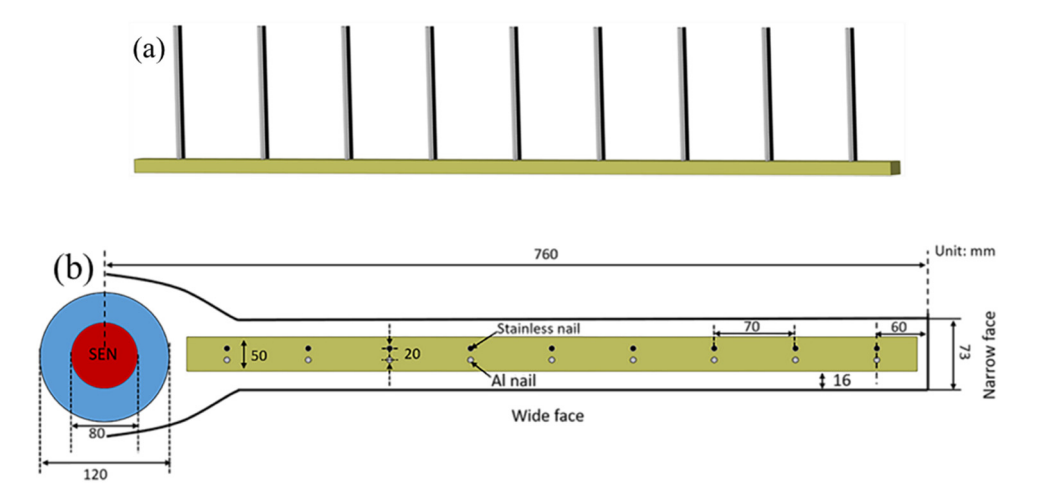
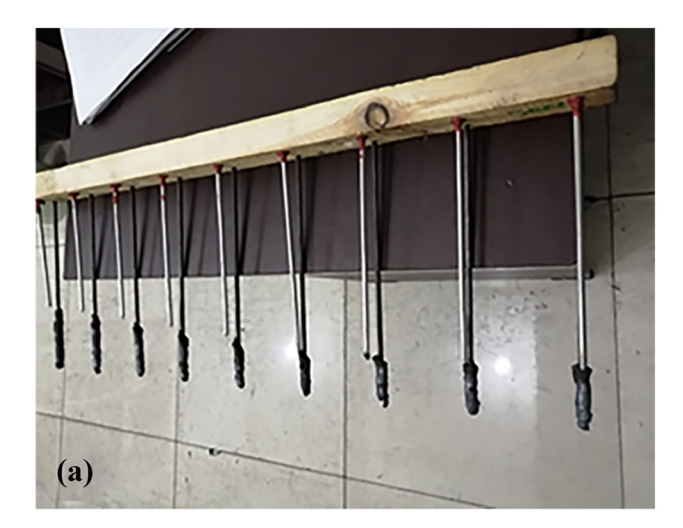


Figure 17: Description of the nail board and position for dipping tests: (a) nail board and (b) position for dipping tests.



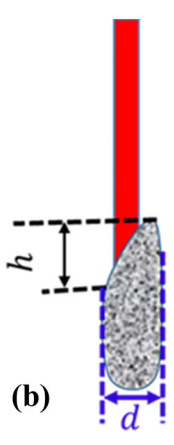


Figure 18: Dipping tests: (a) morphology of nails after dipping tests and (d) solidified steel lumps characteristic parameters.

level has the slag entrapment phenomenon. It also shows that using the FHSEN, whether changing the casting speed or the submerged depth, the maximum value of the surface velocity is larger, and the phenomenon of slag entrapment occurs on both sides of the FHSEN. Therefore, it is a feasible method to optimize the shape of the FHSEN or use the electromagnetic braking technology to change the flow field in the funnel mold [22].

3.2 Numerical simulation of the NSEN

3.2.1 Influence of casting speed on the funnel mold surface velocity

The submerged depth of the NSEN is constant at 130 mm, and the surface velocity distribution of the funnel mold centerline along the funnel mold wide side at casting speeds of 4, 5, and 6 m·min⁻¹ is shown in Figure 11. At different casting speeds, the liquid level centerline of the

surface velocity distributions along the NSEN to narrow face is all sinusoidal half-waveform. And, as the casting speed increases, the flow velocity at the same position gradually increases. At the position of about 450 mm, wave peaks appear at the same time. When the casting speed is 4 m·min⁻¹, the peak value of the surface velocity is the smallest, which is 0.11 m·s⁻¹. It can be seen that when the NSEN submerged depth is constant at 130 mm and the casting speed is in the range of 4-6 m·min⁻¹, the funnel mold surface velocity fluctuates between 0.11 and 0.37 m·s⁻¹, see Figure 12(a)–(c). Compared with the NSEN, the funnel mold surface velocity decreased by 0.19-0.27 m·s⁻¹, and the surface velocity decreased significantly. The reason is that the SEN is submerged in the same depth, and the NSEN outlet is vertically downward and the molten steel stream flows downward vertically, causing the main upper swirl area to be far away from the funnel mold liquid level, leading to the kinetic energy of the upper backflow impinging liquid level to be weakened and hence the surface velocity decreases, see Figure 12(d) and (e). However, when the casting speed is 6 m·min⁻¹, the upwelling speed is large and can reach the liquid level; therefore, the surface velocity has a large gap with the curve of 4 and 5 m·min⁻¹, and the maximum surface velocity moves to the narrow face by about 100 mm.

3.2.2 Influence of submerged depths on funnel mold surface velocity

When the casting speed is constant at 6 m·min⁻¹, the funnel mold surface velocity under different submerged depths is shown in Figures 13 and 14. Figure 13 shows that the velocity distribution of the funnel mold liquid level centerline along the wide face presents a half-sine wave. When the submerged depth is 130 mm, the funnel mold surface velocity is the largest, reaching $0.37 \text{ m} \cdot \text{s}^{-1}$. and when the submerged depth is 190 mm, the funnel mold surface velocity is the smallest, reaching 0.14 m·s⁻¹. Figure 13 shows that the surface velocities for a shallow immersion depth (130 mm) are about three times those for a deep immersion (190 mm). The reason is obvious, the greater the submerged depth of the SEN, the farther the upper swirl zone is from the funnel mold liquid level, resulting in a lower surface velocity. Compared with the FHSEN, when the casting speed is constant at 6 m⋅min⁻¹ and the submerged depth is between 130 and 190 mm, the funnel mold surface velocity decreases by 0.19–0.25 m·s⁻¹. and the surface velocity decreases significantly.

To study whether the funnel mold liquid level of the NSEN is slag entrapment, two-phase VOF simulation was carried out on the slag and molten steel at the maximum

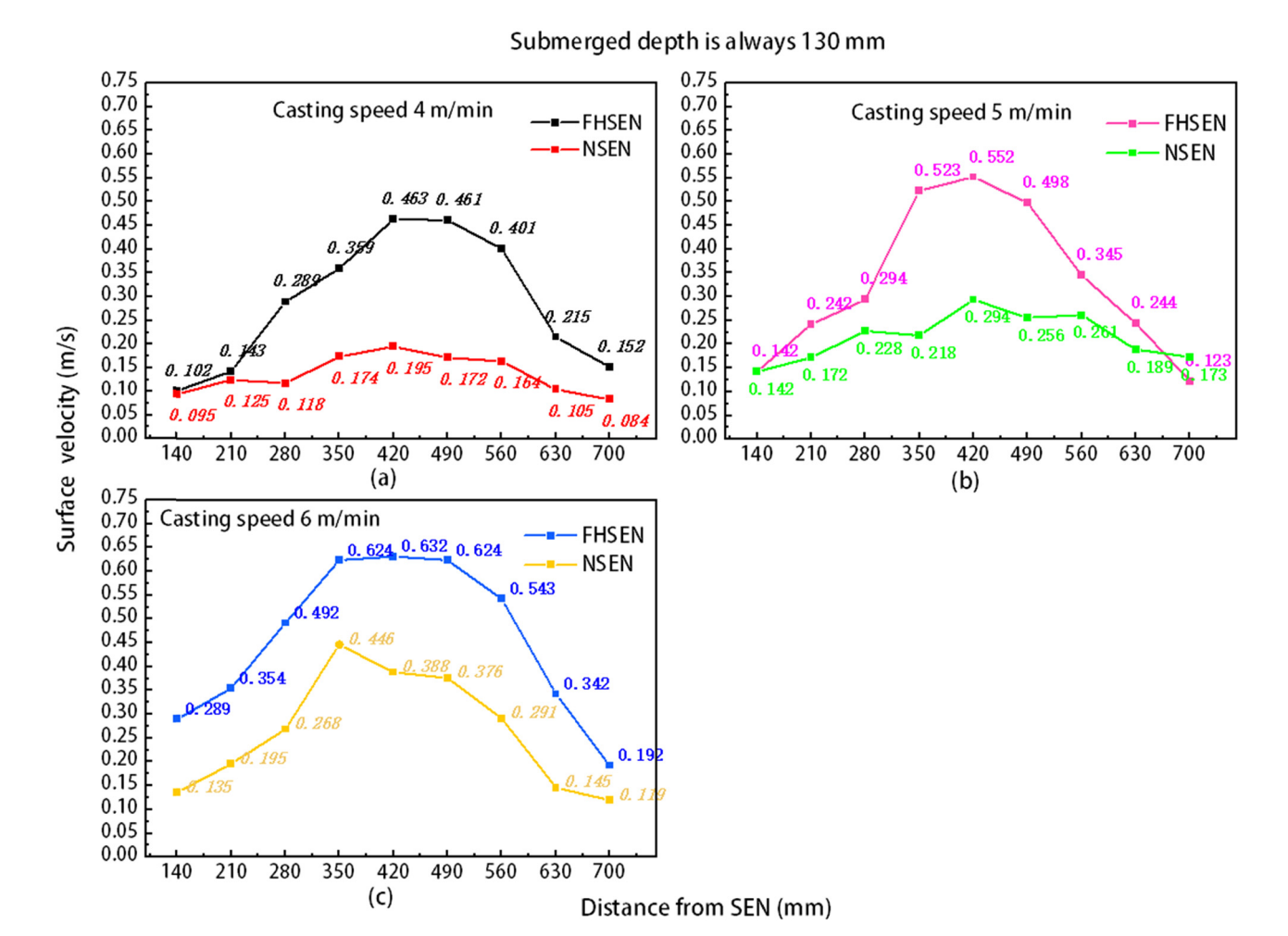


Figure 19: Time-averaged surface velocity by the nail board measurements at a submerged depth of 130 mm: (a) 4 m·min⁻¹, (b) 5 m·min⁻¹, and (c) 6 m·min⁻¹.

surface velocity of the funnel mold liquid level, that is, the NSEN submerged depth is 130 mm and the casting speed is $6 \,\mathrm{m\cdot min}^{-1}$. Under the numerical simulation results of 30 and $60 \,\mathrm{s}$, the slag/steel interface with the slag volume fraction of 0.05% is shown in Figure 15. Figure 15 shows that the interface fluctuation is small and the fluctuation values are within $\pm 6 \,\mathrm{mm}$. In addition, as a result, there is no slag entrainment on the funnel mold liquid level. It can be shown that when the NSEN is used, the probability of slag entrapment on the funnel mold liquid level is very small in the range of the NSEN submerged depths $130-190 \,\mathrm{mm}$ and casting speed $4-6 \,\mathrm{m\cdot min}^{-1}$.

3.3 Industrial test

The effect of different SEN on the funnel mold surface velocity was tested in industry from February to May 2022. The online status of the NSEN is shown in Figure 16.

Using low carbon steel as experimental steel grade, the funnel mold surface velocity was measured at different casting speed and submerged depth by using the nail board. To keep the nails horizontal and stable in the dipping tests, one end of the nails used is inserted into the wood board. Each stainless nail has a length of 150 mm and a diameter of 5 mm, spaced 70 mm apart and attached to the wood board, together with 3 mm diameter aluminum nails. This is shown in Figure 17(a), and the dipping position is shown in Figure 17(b).

During dipping tests, the molten steel solidifies on the nail surface after staying for about 2–3 s and lifting vertically. As molten steel flows around the nails, it is pushed up on the windward side and down on the leeward side, so solidifies an angled lump around each nail. As shown in Figure 18(a), after taking out the nails from the molten steel pool, these solidified steel lumps are used to reveal the liquid level profile and the velocity across the top of the mold. Surface velocity $v_{\rm s}$ (m·s⁻¹) at

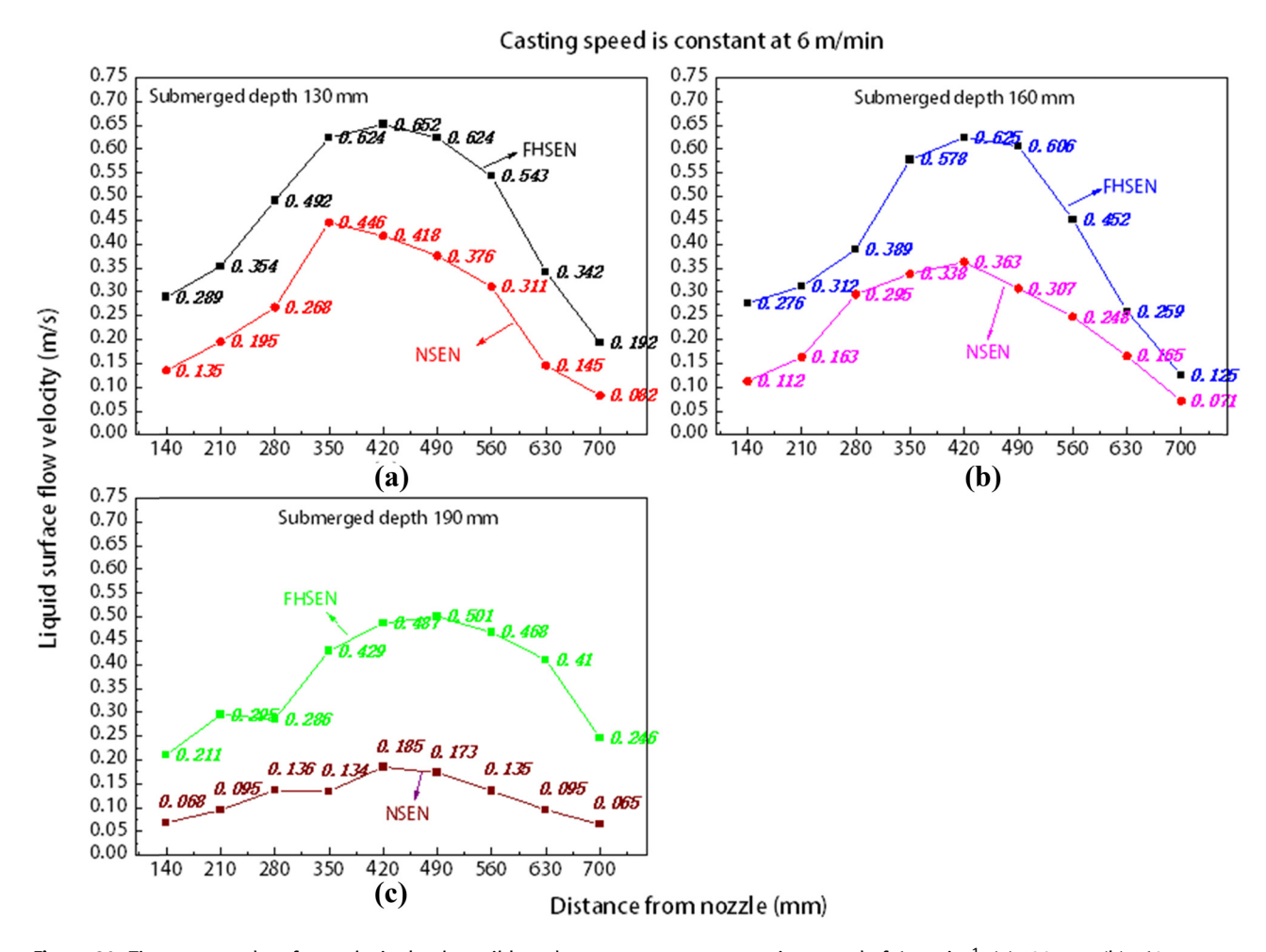


Figure 20: Time-averaged surface velocity by the nail board measurements at a casting speed of 6 m·min⁻¹: (a) 130 mm, (b) 160 mm, (c) 190 mm.

the nail is estimated from the measured lump height difference *h* lump (mm), and lump diameter *d* lump (mm), see Figure 18(b), using the empirical equation (16) developed by Liu et al. [23,24]. Based on the data of computational modeling by Rietow and Thomas [25], for each test, the nail board was dipped into the molten steel for about 3–4 s with 1 min time interval between tests.

$$v_{\rm s} = 0.624 \cdot d^{-0.696} \cdot h^{0.567}$$
 (16)

where v_s is the surface velocity, m·s⁻¹, d is lump diameter, mm, and h is the lump height difference, mm.

Figures 19 and 20 show the funnel mold surface velocity measured with nail board using the FHSEN and NSEN, respectively. See Figure 19, when the SEN submerged depth is constant at 130 mm and the casting speed is within the range of $4-6~\mathrm{m\cdot min}^{-1}$, the funnel mold surface velocity of the FHSEN is significantly higher than that of the NSEN funnel mold, and the maximum funnel mold surface velocity basically occurs at 1/2 of the

distance between the SEN and the narrow face of the funnel mold, and with the increase in the casting speed, the measured funnel mold surface velocity increases. At the same time, as the casting speed is higher, the surface velocity curve of the funnel mold using the NSEN changed from gentle to steeper, indicating that the fluctuation of the surface velocity was intensified; the surface velocity curve of the FHSEN funnel mold fluctuates greatly at low or high casting speed. When the casting speed is 6 m·min⁻¹, the maximum surface velocity measured by the nail board is 0.446 m·s⁻¹, which is 0.186 m·s⁻¹ lower than 0.632 m·s⁻¹ of the FHSEN funnel mold, and the surface velocity decreases significantly. Compared with the numerical simulation results of 0.37 m·s⁻¹, the surface velocity increased by 0.076 m·s⁻¹. At other casting speeds, the measured results are not much different from the numerical simulation results.

Figure 20 shows that when the casting speed is constant at 6 m·min⁻¹ and the submerged depth of the SEN is

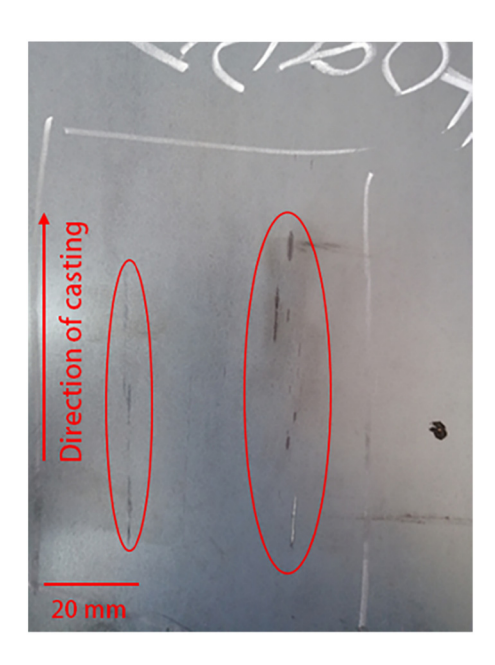
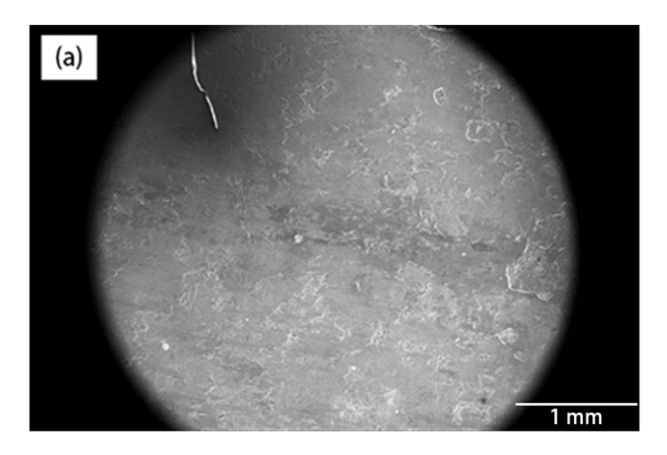


Figure 21: Sliver defects.

in the range of 130-190 mm, the surface velocity of the FHSEN funnel mold is significantly higher than the NSEN funnel mold surface velocity as the SEN submerged depth is larger, the funnel mold surface velocity decreases, and the surface velocity change is becoming more and more gentle. The maximum surface velocity basically appeared in the middle part between the SEN and the narrow face of the funnel mold. The maximum surface velocity of the FHSEN funnel mold fluctuated between 0.481 and 0.652 m·s⁻¹, while the maximum surface velocity of the NSEN funnel mold fluctuates between 0.185 and 0.446 m·s⁻¹, according to refs. 26 and 27. When the surface velocity is less than about 0.38-0.42 m·s⁻¹, the liquid level slag entrapment phenomenon is not easy to occur. Therefore, the NSEN has certain advantages over the FHSEN in controlling the liquid level slag entrapment.

According to the nail board tests, when the SEN submerged depths is 130-190 mm and the casting speed is $4-6 \text{ m}\cdot\text{min}^{-1}$, the maximum surface velocity of the funnel mold using NSEN is $0.446 \text{ m}\cdot\text{s}^{-1}$, which is about $0.206 \text{ m}\cdot\text{s}^{-1}$ lower than the maximum surface velocity of the FHSEN



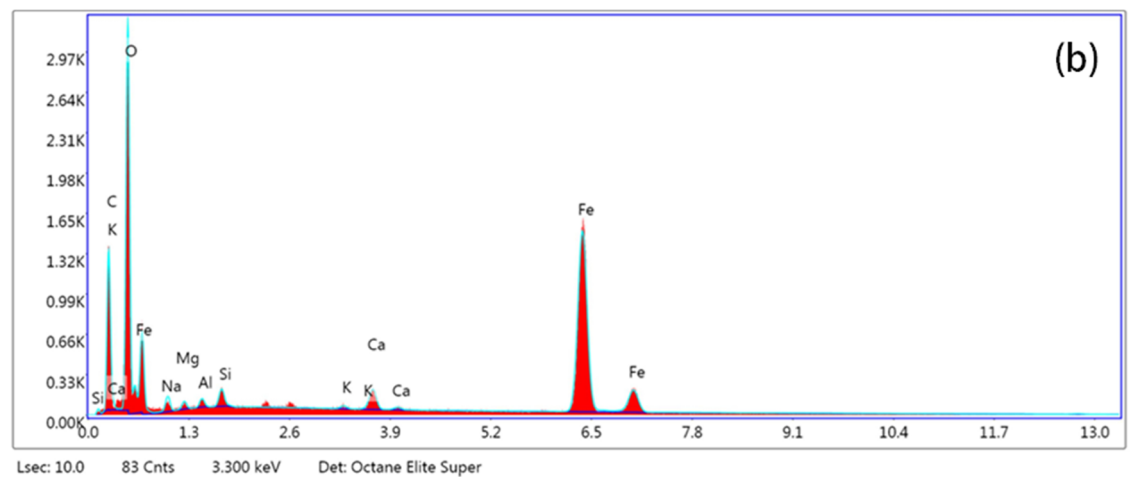


Figure 22: S-3400N scanning electron microscope detection results: (a) morphology and (b) composition.

In addition, in 2021, the sliver defect rate (number of roll coils/total roll coils) caused by slag inclusion was 11.6% for the continuous casting slabs with FHSEN, while the sliver defect rate caused by slag inclusion decreased to 5.8% (86 coils in total) after using the NSEN, and the decrease was obvious. The sliver defects were detected under S-3400N scanning electron microscope, which contained K and Na elements, indicating that the sliver defects contained slags. Typical sliver defects and SEM images are shown in the Figures 21 and 22, respectively. It can be seen that the industrial test results show that the NSEN has certain advantages over the FHSEN in controlling the surface velocity and the slag entrapment caused by the surface velocity. Meanwhile, the reliability of the numerical simulation results is also verified.

4 Conclusion

DE GRUYTER

actual production.

By comparing and analyzing the numerical simulation results of the FHSEN and NSEN, it can be seen that the molten steel at the outlet of the NSEN flows out at a nearly downward vertical angle, and the impact position is deep. After the flow strand collides with the narrow surface of the funnel mold, the upper reflux area is far away from the liquid level of the funnel mold, resulting in the weakening of the kinetic energy when the upper reflux hits the liquid level, compared with the FHSEN, the surface velocity of the NSEN is reduced by 0.19–0.24 m·s⁻¹, and the probability of slag entrapment at the liquid level is also decreased obviously. The industrial test has also proved that the NSEN has lower surface velocity and is not easy to slag entrapment.

Acknowledgments: The authors gratefully acknowledge financial support from the National Natural Science Foundation of China-Regional Innovation and Development Joint Fund key project (U21A20114), the Nature Science Foundations of Hebei Grant (Nos. CXZZBS2020130, E2020209005, and E2019209543), National Natural Science Foundation of China (51904107 and

51974133), Tangshan Talent Subsidy project (A202010004), Science and Technology Research Project of Colleges and Universities of Hebei Province (BJ2019041), and Hebei Province "Three Three Talent Project" supported project (A202010004).

Funding information: This work was funded by National Natural Science Foundation of China-Regional Innovation and Development Joint Fund key project (U21A20114), the Nature Science Foundations of Hebei Grant (Nos. CXZZBS2020130, E2020209005, and E2019209543), National Natural Science Foundation of China (51904107 and 51974133), Tangshan Talent Subsidy project (A202010004), Science and Technology Research Project of Colleges and Universities of Hebei Province (BJ2019041), and Hebei Province "Three Three Three Talent Project" supported project (A202010004).

Author contributions: Limin Zhang: writing-original draft, writing-review and editing, conduct experiment, data, and graphics; Liguang Zhu: project administration, methodology, review, funding, and goals and aims; Caijun Zhang: contacting with the plant and formal analysis; Pengcheng Xiao: contacting with the plant; Xingjuan Wang: funding and review.

Conflict of interest: The authors state no conflict of interest.

Data availability statement: All authors can confirm that all data used in this article can be published the Journal "High Temperature Materials and Processes."

References

- Xing, W. and D. Y. Yuan. Development status and new technology of high-efficiency continuous casting. *Continuous Casting*, Vol. 1, 2011, pp. 1–4.
- [2] Zhu, L. G., L. M. Zhang, and P. C. Xiao. Analysis and control of slag inclusion defects of low carbon steel slab. *Continuous Casting*, Vol. 45, 2020, pp. 36–40.
- [3] Cho, S. M., S. H. Kim, and B. G. Thomas. Transient fluid flow during steady continuous casting of steel slabs: Part I. Measurements and modeling of two-phase flow. ISIJ International, Vol. 54, 2014, pp. 845–854.
- [4] Liu, H., J. Zhang, H. Tao, and H. Zhang. Numerical analysis of local heat flux and thin-slab solidification in a csp funnel-type mold with electromagnetic braking. *Metallurgical Research and Technology*, Vol. 117, 2020, pp. 602–605.
- [5] Weng, Y. M., Y. S. Han, and Q. Liu. Optimization of multi-fields coupled molten steel behavior in bloom continuous casting. *Iron and Steel*, Vol. 53, 2018, pp. 53–60.

- [6] Zheng, S. G. and M. Y. Zhu. Study on mechanism of mould powder entrapment in funnel type mould of flexible thin slab casting machine. *Ironmaking & Steelmaking*, Vol. 41, 2014, pp. 507–513.
- [7] Xu, M. G., H. P. Liu, L. Xiang, and S. T. Qiu. Numerical simulation of transient fluid flow during casting start period in the csp funnel-type mold with electromagnetic brake. *Iron & Steel*, Vol. 49, 2014, pp. 28–33.
- [8] Yang, J., P. Z. Shi, and L. J. Xu. Optimization of submerged entry nozzle structure for 250 mm thick slab mold. *Continuous Casting*, Vol. 44, 2019, pp. 19–25.
- [9] Vakhrushev, A., A. Kharicha, M. Wu, A. Ludwig, G. Nitzl, Y. Tang, et al. Norton-hoff model for deformation of growing solid shell of thin slab casting in funnel-shape mold. *Journal of Iron and Steel Research International*, Vol. 29, 2022, pp. 88–102.
- [10] Li, Z., Y. Xu, and E. G. Wang. Numerical study on behavior of steel/slag interface and fluid flow in electromagnetic continuous casting mold of slab. *Continuous Casting*, Vol. 41, 2016, pp. 1–8.
- [11] Xu, P., Y. Zhou, D. Chen, M. J. Long, and H. M. Duan. Optimization of submerged entry nozzle parameters for ultrahigh casting speed continuous casting mold of billet. *Journal of Iron and Steel Research International*, Vol. 29, 2022, pp. 44–52.
- [12] Wang, H. Q. and Y. P. Bao. Numerical simulation on a slab continuous casting mould. *Journal of University of Science and Technology Beijing*, Vol. 34, 2012, pp. 270–276.
- [13] Zhang, Q. Y. and X. H. Wang. Numerical simulation of influence of casting speed variation on surface fluctuation of molten steel in mold. *Journal of Iron and Steel Research*, Vol. 234, 2010, pp. 15–18.
- [14] Vakhrushev, A., A. Kharicha, Z. Liu, M. Wu, A. Ludwig, G. Nitzl, et al. Electric current distribution during electromagnetic braking in continuous casting. *Metallurgical and Materials Transactions B*, Vol. 51, 2020, pp. 1–18.
- [15] Xu, L. and E. Wang. Numerical simulation of the effects of horizontal and vertical EMBr on Jet flow and mold level fluctuation in continuous casting. *Metallurgical & Materials Transactions B*, Vol. 49, 2018, pp. 2779–2993.
- [16] Jin, X. Study on Fluid Flow Behavior of Molten Steel and Simulation Method in Slab Continuous Casting Mold. PhD theses, Chongqing University, Chongqing, China, 2011.

- [17] Ramirez-Lopez, P. E., P. D. Lee, and K. C. Mills. Explicit modelling of slag infiltration and shell formation during mould oscillation in continuous casting. *ISIJ International*, Vol. 50, 2010, id. 426.
- [18] Chen, W., L. Zhang, Q. Ren, Y. Ren, and W. Yang. Large eddy simulation on four-phase flow and slag entrapment in the slab continuous casting mold. *Metallurgical and Materials Transactions B*, Vol. 53, 2022, pp. 1446–1461.
- [19] Wang, Y., S. Yang, F. Wang, and J. Li. Optimization on reducing slag entrapment in 150 × 1270 mm slab continuous casting mold. *Materials*, Vol. 12, 2019, pp. 1–13.
- [20] Wang, Y., L. Zhang, W. Yang, and Y. Ren. Effect of nozzle type on fluid flow, solidification, and solute transport in mold with mold electromagnetic stirring. *Journal of Iron and Steel Research International*, Vol. 29, 2022, pp. 237–246.
- [21] Wang, W., L. G. Zhu, C. J. Zhang, and Q. Zheng. Water flow field model and numerical simulation of 180 mm × 610 mm slab continuous casting mold. *China Metallurgy*, Vol. 30, 2020, pp. 46–53.
- [22] Garcia-Hernandez, S., R. D. Morales, J. J. Barreto, and K. Morales-higa. Numerical optimization of nozzle ports to improve the fluidynamics by controlling backflow in a continuous casting slab mold. *ISIJ International*, Vol. 53, 2013, pp. 1794–1802.
- [23] Liu, R., J. Sengupta, D. Crosbie, S. Chuang, M. Trinh, and B. G. Thomas. Quantitative measurement of molten steel surface velocity with nail boards and SVC sensor in CC molds. *Proceedings of TMS*, TMS, Warrendale, PA, USA, 2011.
- [24] Wu, X., M. L. Wang, Y. L. Zhang, H. Zhang, and K. F. Zhang. Simulation study on influence factors of flow field in high-speed slab mold. *Steelmaking*, Vol. 36, 2020, pp. 27–33 + 49.
- [25] Rietow, B. and B. G. Thomas. Using nail board experiments to quantify surface velocity in the CC mold. *Proceedings of AISTech*, AIST, Warrendale, PA, USA, 2008.
- [26] Liu, R., B. G. Thomas, J. Sengupta, S. D. Chung, and M. Trinh. Measurements of molten steel surface velocity and effect of stopper-rod movement on transient multiphase fluid flow in continuous casting. *ISIJ International*, Vol. 54, 2014, pp. 2314–2323.
- [27] Wang, J., X. Jin, K. Zhao, J. Peng, J. Xie, J. Chen, et al. Prediction model for steel/slag interfacial instability in continuous casting process. *Ironmaking & Steelmaking*, Vol. 42, 2015, pp. 705–713.